



Design of hierarchical electrocatalytic mediator for one step, selective screening of biomolecules in biological fluid samples

Mohammed Y. Emran^{1,2} · Mohamed A. Shenashen¹ · Adel A. Abdelwahab² · Hesham Khalifa¹ · Moataz Mekawy¹ · Naeem Akhtar¹ · Mohamed Abdelmottaleb² · Sherif A. El-Safty^{1,3}

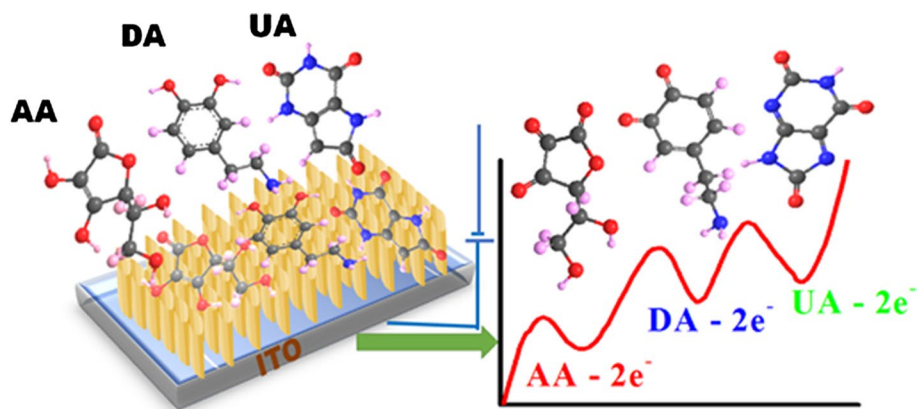
Received: 20 November 2017 / Accepted: 19 February 2018 / Published online: 16 March 2018
© Springer Science+Business Media B.V., part of Springer Nature 2018

Abstract

Active electrocatalytic electrode designs are needed for the sensitive and selective detection of a single or multi-active biomolecule among biological components. We report the design of hierarchical NiO catalyst (HNC) for one-step monitoring of bioactive molecules such as ascorbic acid (AA), dopamine (DA), and uric acid (UA). The novel mesostructured geometries, active surface sites, and multi-diffused spaces for easy electron movement through gaps provide highly active electrocatalytic electrode designing surface. Controlled HNC architecture along electrode-design surface domains having double-head branches spread out along both sides of the dipole-like rod may lead to the vital electron transfer and fast response signaling of multi-bioactive molecules in one-shot triggering individually or simultaneously. Electrochemical analyses showed evidence that the proposed electrode design can detect each component up to 0.02 μM . Sensitive detection up to 1.127, 0.02, and 0.978 μM and wide-range responses of 25–800, 2–60, and 10–000 μM for AA, DA, and UA, respectively, were observed. The simultaneous monitoring and selective signaling of AA, DA, and UA in real urine samples in one step under different potentials were realized. Thus, the HNC-modified electrode can monitor and evaluate the coexistence of biomolecules simultaneously in multi-components.

Graphical Abstract

The electrochemical oxidation of AA, DA, and UA at the HNC-modified electrode and the corresponding DPV peaks with losing of $2e^-/2H^+$.



Keywords Biosensor · Hierarchical NiO · Ascorbic acid · Dopamine · Uric acid, human blood serum · Human urine

Electronic supplementary material The online version of this article (<https://doi.org/10.1007/s10800-018-1175-5>) contains supplementary material, which is available to authorized users.

Extended author information available on the last page of the article

1 Introduction

Monitoring the level of biomolecules, such as uric acid (UA), glucose, ascorbic acid (AA), dopamine (DA), and H_2O_2 , is important in the early warning, detection, control, and provision of useful information for treatment and prevention of various diseases and genetic disorders [1, 2]. For instance, DA plays a key role in many biological and physical processes, such as learning, cognition, locomotion, emotion, and working memory, where its level acts as an indicator of neurological disorders, such as schizophrenia and Parkinson's disease [3, 4]. AA exhibits a vital role in human daily life as a dietary supplement and acts as an antioxidant for prevention of common diseases, such as mental illnesses, common cold, AIDS, and cancer [5]. UA is present in human fluids, such as human urine and serum, where its level is an indicator of some diseases, such as hyperuricemia, gout, and Lesch–Nyhan syndrome [6]. In this context, fabrication of non-enzymatic biosensor for rapid, cost-effective, and on-site monitoring of a wide range of targets has gained increasing interest to revolutionize scientific research. Studies utilized different techniques, including fluorescence microscopy, high-performance liquid chromatography, capillary electrophoresis, and spectrophotometry [7–10].

Electrochemical biosensors have gained increasing attention for detecting bioactive molecules, such as DA, AA, and UA; these sensors exhibit sensitivity, low cost, easy operation, rapid response, handling convenience, qualification for in situ monitoring, excellent compatibility with miniaturization, and good selectivity [11–13]. The performance of electrochemical biosensors is considerably affected by the interface structure and properties of the target [14]. A reliable analytical method for one-pot measurement of DA, AA, and UA levels in biological samples should be established. Simultaneous detection of bioactive molecules on commercial electrodes is difficult because of usual interference and overlapping of the electrode signal [11–15]. Therefore, interface modification largely influences the performance of electrochemical sensors.

Numerous studies reported on interface modification for simultaneous detection of biomolecules [16–20]. Scholars have developed Pt/reduced graphene oxide (Pt/RGO), 3D porous graphene, polydopamine/multiwall carbon nanotube (MWCNT), poly(L-methionine)/AuNPs/GCE, one-dimensional carbon nanomaterial, and flower-like ZnO-decorated polyaniline/RGO nanocomposite for detection of DA and UA in the presence of AA [21–26]. Other modifiers have also been synthesized for simultaneous detection of AA, DA, and UA; these modifiers include size-selected Pt@graphene/nanocomposites, NiCo/N-carbon nanoplates, cetyltrimethylammonium bromide-functionalized

graphene oxide/MWCNT composites, N-doped carbon nanotubes, and Fe_3O_4 nanoparticles, activated graphene/MWCNT nanocomposite-loaded Au nanoclusters, flexible graphene fiber functionalized by $NiCo_2O_4$ nanowires, and RGO–zinc oxide composites [16–20, 27, 28]. Thus, future works must develop electrochemical biosensors for highly sensitive simultaneous detection of coexisting bioactive molecules by using low-cost materials and simple synthesis and fabrication methods.

Transition metal oxides possess intrinsic features, such as high surface area, easy and low-cost preparation, environmental friendliness, structure flexibility, and excellent mechanical and chemical properties; hence, these oxides are a promising choice as an electrochemical mediator [29–37]. NiO with different structures exhibits advantages, such as lower cost, nontoxicity, and higher resistance to corrosion, compared with other derivatives, such as gold, platinum, palladium, and rare-earth nanoparticles [38–42]. NiO also exhibits electron delocalization between adjacent Ni^{2+} and Ni^{3+} ions and promotes fast electron transfer between the electrodes and the active site of the redox biological reaction [43]. NiO possesses different morphological structures, such as dendritic NiO@carbon–nitrogen dot and hierarchical NiO nanostrand, which exhibit distinct electrocatalytic performance suitable for non-enzymatic glucose biosensor, and detection of mono-bioactive molecules [40–43].

In this study, hierarchical NiO catalyst (HNC) is synthesized through one-pot hydrothermal treatment and used for simultaneous monitoring of AA, DA, and UA. HNC exhibits a distinct morphology with specific features, and its structure can be described as two similar heads connected by a rod-like dipole. Each head consists of thick nanotubes on its surface and features high surface area, multi-active sites, smooth surface, and pores inside the surface and between lattices. The HNC is used to modify an electroactive electrode for catalytic oxidation of bioactive molecules with enhanced sensitivity and selectivity. The HNC-modified electrode exhibits sensitive and selective electrooxidation of DA, AA, and UA individually or simultaneously in one pot. The HNC-modified electrode can be used to monitor and evaluate single or multiple molecules in human fluid samples (human serum and urine) for clinical application.

2 Experimental

2.1 Synthesis of HNC

HNC was prepared by the one-pot hydrothermal synthetic approach. $Ni(NO_3)_2 \cdot 6H_2O$ (1 mM) was dissolved in 100-mL volumetric flask that contained 20 mL of deionized water with vigorous stirring until clear. Consequently, homogeneous solution was obtained at room temperature.

Approximately 20 mL of $(\text{NH}_4)_2\text{HPO}_4$ (1 mM) dissolved in deionized water was added to the previous solution under stirring. Subsequently, the solution mixture was transferred into a 100-mL Teflon-lined stainless-steel autoclave, sealed, and maintained at 160 °C for 8 h. The green precipitate was filtered using a centrifuge and washed with water/ethanol to remove the soluble impurities. The HNC was dried in an oven at 80 °C and annealed at 400 °C for 4 h.

2.2 Material characterizations

High-resolution transmission electron microscopy (HR-TEM), scanning transmission electron microscopy (STEM), electron diffraction (ED), and energy-dispersive X-ray spectroscopy for elemental mapping (STEM-EDS) were performed using a JEOL JEM model 2100F microscope. N_2 adsorption-desorption isotherms were measured at 77 K using a BELSORP36 analyzer (JP. BEL Co., Ltd.). The structural geometry of the catalysts was further examined by WA-XRD. The WA-XRD patterns were recorded using an 18 kW diffractometer (Bruker D8 Advance) at a scan rate of $10^\circ \text{ min}^{-1}$ with monochromatic $\text{Cu K}\alpha$ -X-radiation ($\lambda = 1.54178 \text{ \AA}$). XPS analysis was conducted on a PHI Quantera SXM (ULVAC-PHI) instrument (Perkin-Elmer Co., USA) equipped with $\text{Al K}\alpha$ as an X-ray source for excitation ($1.5 \text{ mm} \times 0.1 \text{ mm}$, 15 kV, and 50 W) under a pressure of $4 \times 10^{-8} \text{ Pa}$. Raman spectroscopy (HR Micro Raman spectrometer, Horiba, Jobin Yvon) was conducted using an Arion laser at 532 nm.

2.3 Fabrication of working electrode

The modified ITO electrode was fabricated as follows. The synthesized HNC (5 mg mL^{-1}) was dispersed in 5 mL of methanol at room temperature. The HNC/ITO was designed by spreading 20 μL of HNC on the surface of ITO glass substrate ($2 \text{ cm} \times 1 \text{ cm}$). To control the exposed surface area of ITO substrate and improve the electrical contact, a definite area ($1 \text{ cm} \times 1 \text{ cm}$) of the ITO electrode substrate was masked prior to the deposition. This process was repeated five times. The resulting electrode was dried overnight at room temperature and washed with deionized water to remove any unbound particle.

2.4 Electrochemical sensing system

Zennium/ZAHNER-Electric instrument that was controlled by Thales Z 2.0 software at room temperature was used for all electrochemical measurements. A three-electrode system containing ITO glass modified ($2 \text{ cm} \times 1 \text{ cm}$) as working electrodes, platinum wires as a counter electrode, and Ag/AgCl (3 M NaCl) as a reference electrode was used for electrochemical analysis. The freshly prepared electrolyte (0.1 M

PBS) was de-aerated by bubbling a slow stream of purified N_2 to avoid DA oxidation. The N_2 flow was maintained during the entire electrochemical measurements to ensure N_2 -saturated electrolyte.

2.5 Biological fluid sample analysis using HNC-modified electrode

The real application was performed using standard addition in human blood serum and urine samples. Urine samples were collected from three different volunteers during their first urination after night time. A control test was also performed using standard addition. Human urine samples were diluted 5 times by using phosphate-buffered saline (PBS) (0.1 M, pH 7.0). Approximately 500 μL of the diluted urine sample was added to 9.5 mL of PBS (0.1 M) solution for differential pulse voltammetry (DPV) experiments under an N_2 -saturated atmosphere at room temperature. The human blood serum sample was prepared as follows. 10 μL of human serum was added to 10 mL of PBS (pH 7). Then known concentrations of AA, DA, and UA were added to the prepared samples and electrochemically measured using DPV in the potential range of 0–0.7 V at a pulse height of 60 mV, pulse width of 25 mV, pulse distance of 200 ms, and a step height of 5 mV, each experiment was repeated three times under N_2 flow.

3 Results and discussion

3.1 Synthesis of HNC

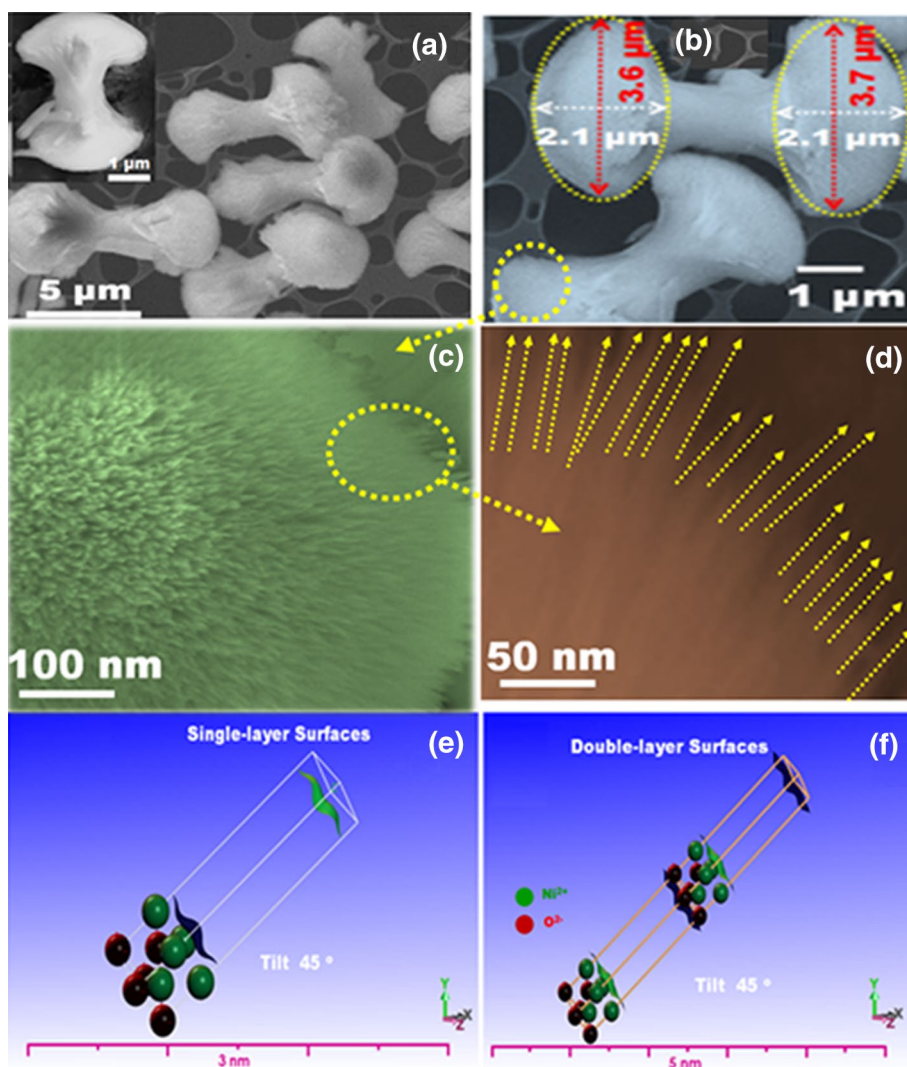
A controlled fabrication of a morphological structure with multifunctional active sites as electrocatalyst was performed. This structure possesses (i) multi-active sites on the contact surface, (ii) highly ordered crystalline facets with low energies for binding and adsorption (iii), intensive charge density at the surface streams, and (iv) electron accumulation, cloud, or dense growth at the surface.

Scheme S1 shows a simple, one-pot synthesis of HNC surface decorations that is longitudinally constructed from their head and rod. Simple one-pot hydrothermal treatment of composition $(\text{Ni}(\text{NO}_3)_2)/(\text{NH}_4)_2\text{HPO}_4/\text{H}_2\text{O}$ domains results in the formation of the macro unit of NiO with two heads connected by a rod, which is like a dipole. The construction of each head provides highly active characteristic features obtained from the thick nanotube spread on the outer sites with open pores and cavity ends (Fig. 1a, b).

3.2 Structure featured of HNC

Field effect-scanning electron microscope (FE-SEM) and high-resolution transition microscope were used to

Fig. 1 **a** The low FE-SEM magnification images of HNC, which illustrate the surface morphology and symmetric double-head distribution. Inset of **a** the FE-SEM focusing on the one unit structure of the HNC. **b** The FE-SEM image of HNC focusing on the construction and configure the size of head and rode. The head surface construction observed from the high magnification of FE-SEM focused on the head (**c, d**). Crystal surfaces and atomic configuration of Ni^{2+} , and O^{2-} for single-layer surfaces (**e**), and double-layer surfaces (**f**) along the entire exposed $\{111\}$ -surface plane, particularly at the 4-Ni^{2+} -top surfaces



investigate the geometrical and morphological structures of the synthesized materials. The HNC morphological structure exhibits rhythmic dual-head spread out along with dipole-like rod between two symmetric heads, as indicated in the FE-SEM micrograph (Fig. 1a, b). The head geometry is like an umbrella construction with an average size 3–4 μm ; these heads were connected by a rod with an average size of 1.5–2 μm (inset of Fig. 1a). Figure 1c, d illustrates the head morphologies and provides a specific structure where the outer surface is a rough jagged surface. As illustrated in Fig. 1a–d; novel geometrical constructions with rhythmic head construction were designed. Furthermore, the atomic configuration of NiO using DFT theory implies the complete surface construction with contact active sites with targeted molecules. Figure 1e, f represents the atomic configuration of HNC crystal along single-layer- and double-layer-exposed $\{111\}$ surface plane. The $\{111\}$ -top surface around double-layer provides high energy of electron surfaces along the entire HNC crystal structure, which is directed along

$\{111\}$ surface exposure, particularly at the top 4-Ni^{2+} surfaces. Consequently, the electrocatalytic activity of Ni^{2+} with the target molecules is enhanced and the exposure contact catalytic active sites are high. Furthermore, the electrostatic potential mapping of the $\{111\}$ -exposed plane surfaces strongly suggests that the top surface of Ni^{2+} and O^{2-} atoms near the vacancy sites are charged surfaces. The surface-representing localized networks, which elevated to antedate the surface charge density around O and Ni atoms and the effective potential differences of AA, DA, and UA overlapping with Ni^{2+} site binding.

The head construction of the HNC was further provided by HAADF-STEM image in Fig. S1. The high-resolution HAADF-TEM illustrates that the head surface contains a thick nanotube at its end (Fig. S1a); the nanotube's size is approximately 20 nm. Figure S1b, c shows the HAADF-STEM image of nanotubes and provides the porous structure of the HNC. The nanotubes exhibit a uniform structure with pore distance of around 10 nm and

smooth surface. Highly crystalline order of HNC is shown in HAADF–STEM images (Fig. S1d, and inset of S1b). The lattice distance is 1.476 Å, which corresponds to the d_{111} spacings in the XRD pattern. The high-magnification HAADF–STEM image of HNC at the nanotubes surface and along the {111}-crystal plane (Fig. S1d). The ED-STEM image (inset of Fig. S1b) shows the abundant resolutions of low- and high-index lattice planes of (2–20), (20–2), (0–22), (02–2), (–202), and (–220) fringes around the {111}-principle zone-dominant plane. These results also indicate that all the nanotubes in the head of NiO display the same orientation along the {111} direction.

Surface nature was investigated using N_2 adsorption–desorption isotherms (Fig. 2a). The HNC features a specific surface area (S_{BET}) of $22.3 \text{ m}^2 \text{ g}^{-1}$, as well as the NLDF analysis was used to confirm the pore size distribution as shown in the inset of Fig. 2a. The obtained results reflects the hierarchical structure of NiO (meso- and microporous distribution) surfaces [44–50]. The HNC provides high surface area as compared to other NiO-based materials such as NiO nanoplates, NiO nanoslices, and dendritic NiO, where their surface areas are 20.2, 11.4, and $5.06 \text{ m}^2 \text{ g}^{-1}$, respectively [43, 51–53]. Sharp

and well-resolved diffraction peaks of NiO sample were observed in the wide-angle X-ray diffraction patterns (Fig. 2b). The diffraction peaks at 37.2° , 43° , 63° , 75.5° , and 79.6° correspond to the (111), (200), (220), (311), and (222) planes, respectively, of the face-centered cubic (fcc) lattice structure of NiO [54]. Further confirmation by matching with JCPDS No. 01-089-5881 illustrates the fcc Fm3m symmetry with the lattice constant a of 8.35 Å.

The Raman spectrum of the HNC sample shows several bands above 400 cm^{-1} at the excitation wavelength of 532 nm (Fig. 2c). The Raman spectra of HCN show a vibrational band at approximately 532, 760, and 1085 cm^{-1} due to one phonon optical mode and two phonons, indicating the presence of pristine NiO [54]. X-ray photoelectron spectroscopy (XPS) measurements were performed to elucidate the surface features and components of NiO. Figure 2d shows the XPS spectra of NiO. In addition, the high-resolution XPS spectra of the O 1s and Ni 2p peaks are shown in Fig. S2a, b, respectively. Two main peaks centered at 872.3 and 854.3 eV are related to the Ni 2p¹ and Ni 2p³ of Ni(II) ions, respectively (Fig. S2b) [55]. The peak of O 1s in the HNC visibly shifts to lower binding energy than that of pristine NiO (Fig. S1a).

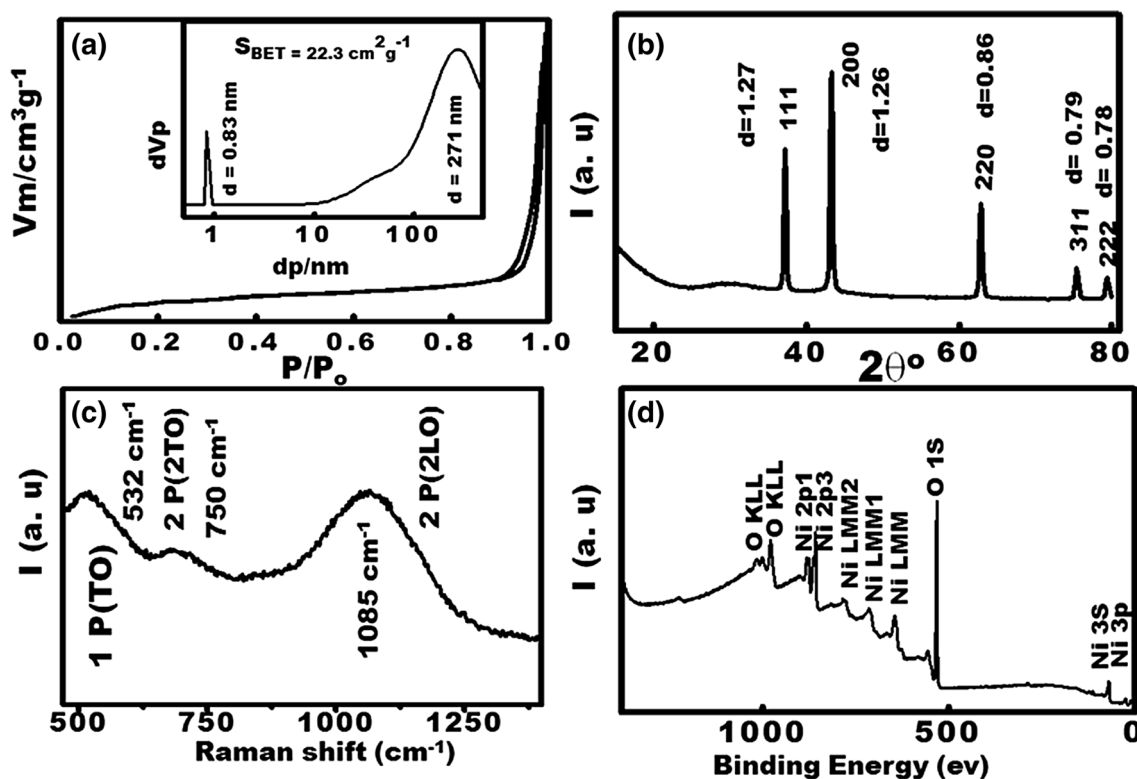


Fig. 2 N_2 adsorption–desorption isotherms (a), XRD pattern (b), Raman spectrum (c), XPS spectrum (d) of HNC. (Inset of a) the NLDF model for pore size distribution of the HNC with the surface

properties data of the specific surface area of $S_{BET}/\text{m}^2 \text{ g}^{-1}$, NLDF pore (d, nm), and pore volume ($V_p, \text{cm}^3 \text{ g}^{-1}$), respectively

3.3 Electrochemical mode of HNC-modified electrode

The actively catalytic surface and the electron transfer quality of the nanoelectrode (HNC/ITO) were investigated using cyclic voltammetry (CV) test in 0.1 M KCl containing 0.1 mM $[\text{Fe}(\text{CN})_6]^{3-}$ with applied potential ranging from 0.0 to 0.7 V (vs. Ag/AgCl) at a scan rate of 100 mV s^{-1} (Fig. S3a). The electrochemical activity of the modified electrode and charge transfer mobility on the surface were elucidated using $[\text{Fe}(\text{CN})_6]^{3-}$ as a redox probe [56]. The high ion diffusion at the electrode–electrolyte interface and the excellent performance of the catalytic active sites were observed from the peak behavior of $[\text{Fe}(\text{CN})_6]^{3-}$. The peak-to-peak separation (ΔE_p) values exhibit a characteristic value for electron transfer speed on the electrode surface, and the oxidation peak current reflects the electrode catalytic power. The ΔE_p values of the HNC-modified electrode and bare electrodes are 108 and 186 mV, respectively. The oxidation peak of the HNC-modified electrode is fourfold greater than that of the bare electrode. Thus, the HNC-modified electrode exhibits high catalytic performance and high electron transfer [57, 58].

The electrochemical constants such as charge transfer coefficient (α) and electron transfer rate constant (K_s) were calculated for the ITO and HNC/ITO. Figure S3b, c shows the plot of $\log \nu$ (scan rate ranged from 50 to 300 mV s^{-1}) versus the anodic (E_a) and the cathodic (E_c) applied potential of 0.1 M $[\text{Fe}(\text{CN})_6]^{3-}$ in 0.1 M KCl at ITO and HNC/ITO. The anodic applied potential E_a and cathodic applied potential E_c were linearly proportional to $\log \nu$. The regression equations for the HNC/ITO are $E_a(\text{V}) = 0.44 + 0.022 \log \nu$ (V s^{-1}), ($R^2 = 0.996$) and $E_c(\text{V}) = 0.29 - 0.021 \log \nu$ (V s^{-1}) ($R^2 = 0.991$). By applying Laviron's theory [59], the charge transfer coefficient (α) was calculated and found to be 0.51, according to the calculated values of the slopes of the linear relationships of E_a and E_c versus $\log \nu$, as shown in the following equation:

$$\log K_a/K_c = \log \alpha/(1 - \alpha) \text{ or } K_a/K_c = \alpha/(1 - \alpha), \quad (1)$$

where K_a is a constant that determines from the slope of E_a versus $\log \nu$ and equals to $2.3 RT/(1 - \alpha)nF$, K_c is a constant that determines from the slope of E_c versus $\log \nu$ and equals to $-2.3 RT/\alpha nF$, R is the gas constant, F is the Faraday constant, and T is the absolute temperature.

The electron transfer rate constant (K_s) in heterogeneous electrolyte–electrode surface assays can be calculated by applying this equation [43]:

$$\log K_s = \alpha \log (1 - \alpha) + (1 - \alpha) \log \alpha - \log \frac{RT}{nF\nu} - \frac{\alpha(1 - \alpha)nF\Delta E_p}{2.3RT}, \quad (2)$$

where n is the number of electrons evolved in the reaction, α is the charge transfer coefficient, ν is the scan rate (V s^{-1}), ΔE_p is the peak separation potential between anodic and cathodic peak potentials (V), R is the gas constant ($\text{J K}^{-1} \text{mol}^{-1}$), F is the Faraday constant (J mol^{-1}), and T is the absolute temperature (K).

Result shows that the K_s value was calculated to be 0.769 s^{-1} . In addition, the rate charge transfer coefficient (α), and heterogeneous rate constant (K_s) for the ITO electrode were found to be 0.674, and 0.456 s^{-1} , respectively. These results indicated that the HNC-modified electrode has higher charge transfer than that of bare ITO electrode.

Electrochemical impedance microscopy (EIS) was used to provide efficient electron transfer and electrocatalytic activity on the HNC-modified electrode surface. The EIS curve shows two efficient props, namely, (i) the semicircle diameter indicates the electron resistance of the electrode at high frequencies and (ii) the line reflects electron diffusion at low frequencies [60]. Figure S3d shows typical Nyquist impedance plots of HNC-modified electrode and ITO electrodes in 0.1 M PBS (pH 7.0). The HNC-modified electrode shows a shorter semicircle diameter at high frequency than that of the ITO electrode, thereby showing a relatively small R_{et} . The semicircle of the HNC-modified electrode further decreased with remarkably low R_{et} value and high conductivity. These results indicate that the HNC-modified electrode possesses highly catalytic active surface with enhanced electron transport efficiency.

3.4 Electrocatalytic behavior of AA, DA, and UA on HNC-modified electrode

The electrocatalytic activity of the HNC-modified electrode toward the electrooxidation of AA, DA, and UA was investigated using CV method in PBS solution (pH 7) with and without the target biomolecules. The biomolecules oxidized on the surface of the HNC and lost $2e^-/2H^+$ within the pH studied (Scheme S2). Figure 3a shows an oxidation peak at approximately 0.19 V in the presence of AA (500 μM) in 0.1 M PBS (pH 7) at a scan rate 100 mV s^{-1} . This peak is related to the oxidation of the functional groups at AA from hydroxyl to carbonyl in furan ring form on the HNC-modified electrode surface [61–63]. DA exhibits redox peaks at 0.24 and 0.2 V on the HNC-modified electrode (Fig. 3b). This couple of redox peaks results from DA oxidation to *o*-quinone and the reduction of *o*-quinone to DA with low separation potential value [$\Delta E_p (E_a - E_c) = 0.046 \text{ V}$]. Consequently, DA presents high electrocatalytic response and effective electron transfer [16, 62–64]. Figure 3c shows that UA (200 μM) displays an oxidation peak at 0.354 V and a reduction peak at 0.331 V. The presence of these two peaks may be related to the redox reaction of UA and its quinoid form on the HNC [63–65].

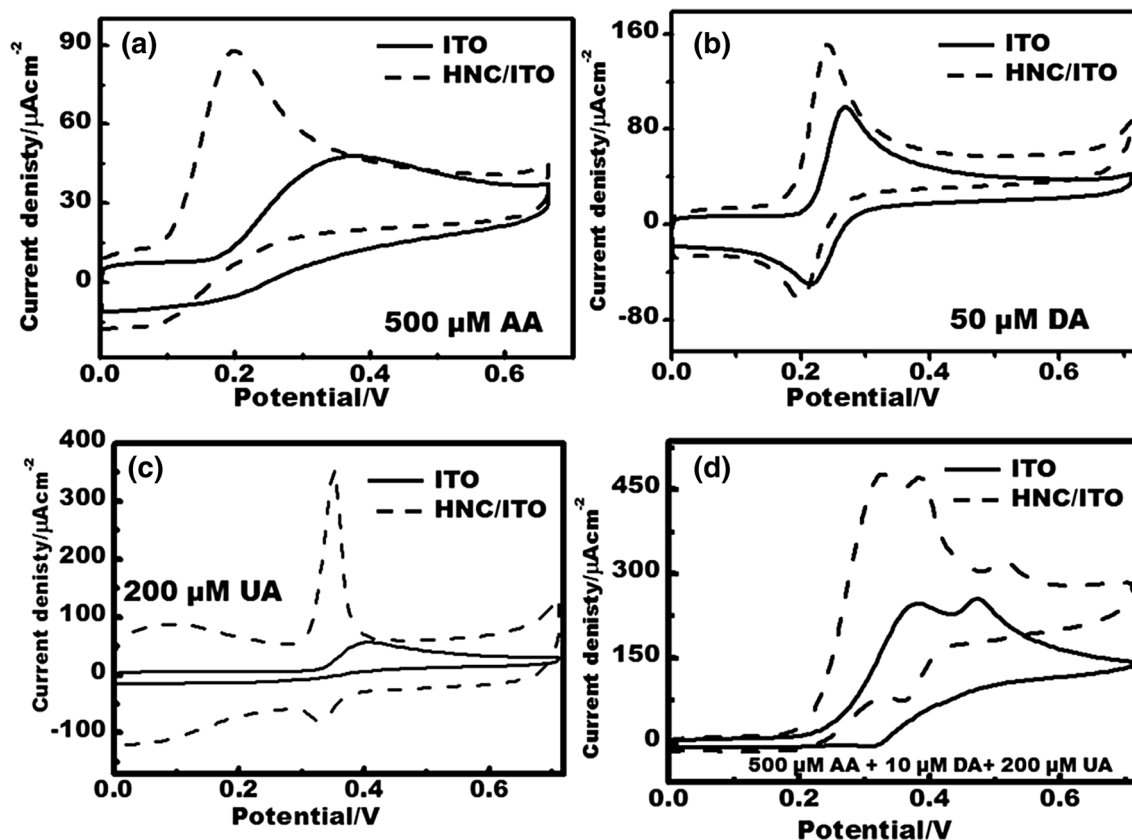


Fig. 3 CVs of HNC-modified electrode and bare ITO electrodes during the detection of 500 μM AA (a), 50 μM DA (b), 200 μM UA (c), and 500 μM AA + 10 μM DA + 200 μM UA (d) in N_2 saturated of 0.1 M PBS (pH 7) at scan rate of 100 mV s^{-1}

As shown in Fig. 3d, the CV curves of AA (500 μM), DA (10 μM), and UA (200 μM) in 0.1 M PBS (pH 7) at the ITO electrode indicate one broad peak at approximately 0.375 V. This peak belongs to AA and DA. These results demonstrate that ITO cannot determine AA and DA concentrations in one pot. Figure 3d indicates the following: (i) the current response of HNC-modified electrode is larger than that of ITO, which is related to the high sensitivity of the modified electrode, and (ii) a three well-defined peaks at HNC-modified electrode in the presence of the three bio-molecules indicate the possibility of monitoring coexisting bioactive molecules in one pot. The HNC-modified electrode illustrates honest peak potentials at 0.28, 0.336, and 0.448 V for AA, DA, and UA, respectively. The $\Delta E(\text{V})$ between the oxidation peaks of AA–DA, AA–UA, and DA–UA is 0.056, 0.168, and 0.112 V, respectively. The morphological and chemical compositions of HNC play a key role in the simultaneous detection of AA, DA, and UA molecules in PBS (pH 7). The HNC electrode with controllable head construction and rod expressing a geode hierarchy along the {111} crystal facets might result in suitable accommodation for trapping and multi diffusivity of different coexisting bioactive molecules into open-pore holes and caves with connective open

macro/meso windows of NiO geodes. The finding confirms that the designed modified HNC electrode can monitor and evaluate the coexistence of AA, DA, and UA in one pot through electrochemical measurement with high sensitivity and selectivity.

The supporting electrolyte pH effects on the electrochemical behavior of AA, DA, and UA at the HNC-modified electrode are illustrated by cyclic voltammogram (CV) in the pH range of 6–8 for AA and UA, and 4.0–9.0 for DA. As a variation of pH solution, the oxidation–reduction peak potentials shifted to a negative value as a result of proton participation of the electrooxidation of detected bioactive molecules as shown in Fig. 4a, c, and e. A linear relationship was observed by plotting pH versus the applied potential (V) with regression equations: $E_{\text{pa}}(\text{V}) = 0.34 - 0.024 \text{ pH}$ ($R = 0.97$), $E_{\text{pa}}(\text{V}) = 0.46 - 0.047 \text{ pH}$ ($R = 0.94$), and $E_{\text{pa}}(\text{V}) = 0.7 - 0.051 \text{ pH}$ ($R = 0.97$) for AA, DA, and UA, respectively (Fig. 4b, d, f). These results showed that the overall oxidation reaction involves a proton.

According to the straight line in Fig. 4b, d, f, the slopes of lines are -0.047 , -0.024 , and -0.051 for DA, AA, and UA, respectively. This observation implies that the value of m (number of protons) is equal to that of n (electron

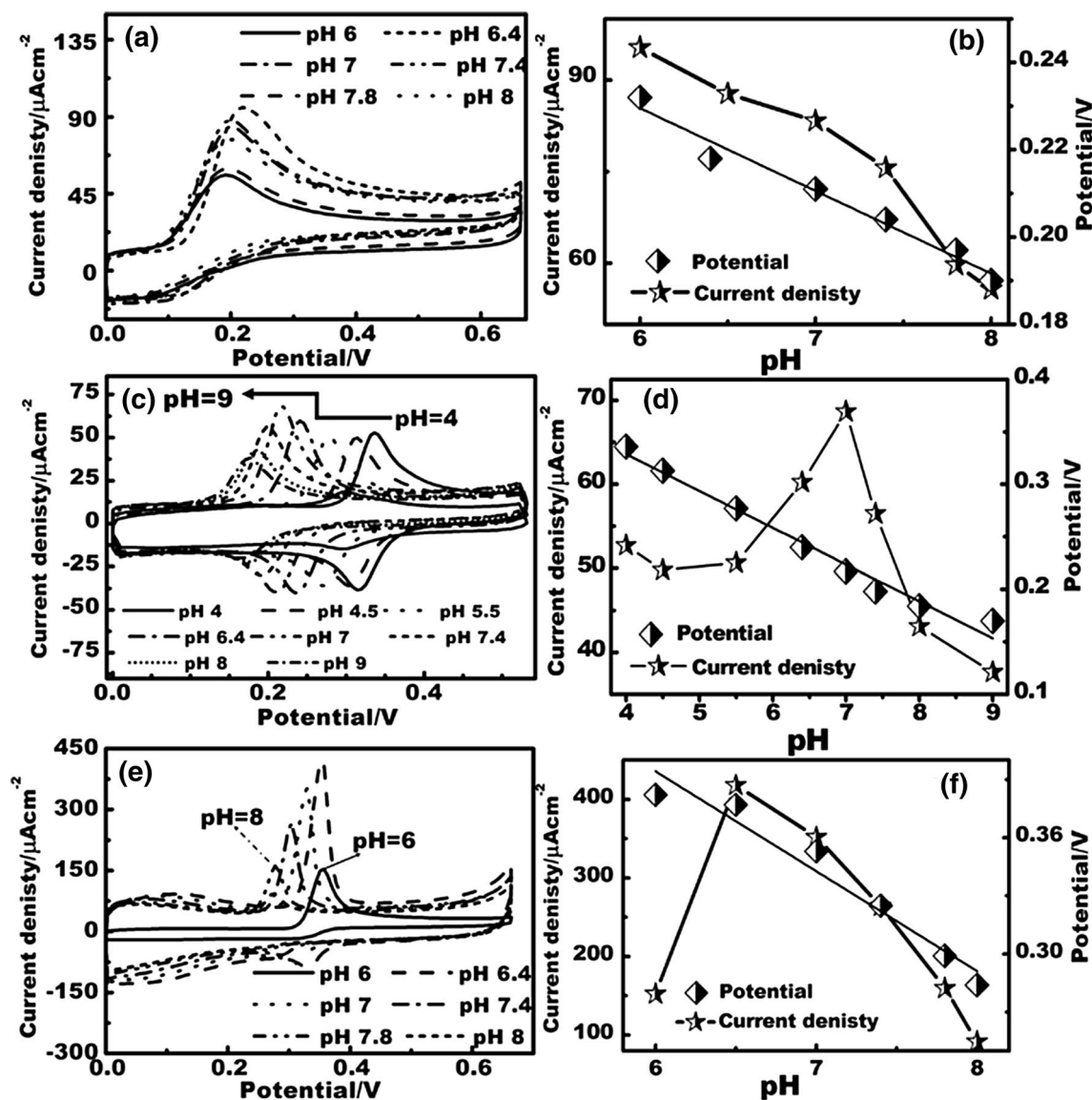


Fig. 4 CVs of pH-dependent monitoring assay of 500 μM AA in different pH values ranged from pH 6–8 (a), 50 μM DA in different pH values ranged from pH 4–9 (c), and 200 μM UA in different pH values ranged from pH 6–8 (e) using HNC-modified electrode under N_2 -saturated at scan rate 100 mV s^{-1} and 25°C . The linear-, and

scatter-plots of applied potential (V) (points), and the anodic current density ($\mu\text{A cm}^{-2}$) (scatter) of 500 μM AA (b), 50 μM DA (d), and 200 μM UA (f) using HNC-modified electrode at different pH solutions under N_2 saturated

transfer number) and further confirms the validity of mechanism, that is, the $2\text{e}^-/2\text{H}^+$ reaction of DA, UA, AA [62–65]. Moreover, the oxidation peak currents of AA decrease with variable pH solution ranging from 6.0 to 8.0 (Fig. 4a). The oxidation peak current of DA gradually increases with increasing solution pH in the range of 4.0–7.0 and decreases when pH exceeds 7.0 (Fig. 4c). The oxidation peak current of UA decreases in the pH range of 6–6.5, increases at pH 7, and then decreases gradually until pH 8 (Fig. 4e). Based on these results, 0.1 M PBS (pH 7.0) is the optimum pH solution, which is near physiological conditions.

The electrochemical kinetics on the electrode surface, namely, diffusion or adsorption-controlled process, can be obtained by studying the effect of scan rate. Fig. S4c shows the CVs of varying scan rate at the HNC-modified electrode for DA (50 μM) in PBS (0.1 M, pH 7). The anodic and cathodic peak currents increased proportionally in both sides with increasing scan rate from 50 to 300 mV s^{-1} . The plot of oxidation and reduction peak currents versus the square root of scan rate is linear with regression equations (i) anodic equation, $I_a (\mu\text{A cm}^{-2}) = -123.15 + 39.75 \nu^{1/2} (\text{mV s}^{-1})$ ($R^2 = 0.996$), and (ii) cathodic equation, $I_c (\mu\text{A cm}^{-2}) = 119.38 - 37.16 \nu^{1/2} (\text{mV s}^{-1})$ ($R^2 = 0.994$)

(Fig. S4d). These results indicate that the oxidation–reduction of DA at HNC is controlled by the diffusion-controlled process [16–20]. Subsequently, the controlling mechanism of AA and UA at HNC-modified electrode was studied by varying the scan rate from 50 to 300 mV s^{-1} in PBS (0.1 M, pH 7) using CV, as presented in Fig. S4a, e. The oxidation peak current of AA increased with the increasing of scan rate from 50 to 300 mV s^{-1} . A linear relation is illustrated by plotting the anodic peak current versus scan rate at, where the regression equation is $I (\mu\text{A cm}^{-2}) = 3.6 + 0.046 \nu (\text{mV s}^{-1})$, $R^2 = 0.98$ for 500 μM AA in PBS (0.1 M, pH 7) (Fig. S4b). This relation indicates that the AA oxidation at the HNC-modified electrode is an adsorption-controlled process. By contrast, the linear relationship of UA between the square root of the scan rate and the anodic current was obtained, where the regression equation expressed as $I (\mu\text{A cm}^{-2}) = 3.6 + 0.046 \nu^{1/2} (\text{mV s}^{-1})$, $R^2 = 0.97$ for 200 μM UA in PBS (0.1 M, pH 7). This result reveals that overall oxidation of UA at the HNC-modified electrode is a diffusion-controlled process (Fig. S4f).

3.5 One-step monitoring of AA, DA, and UA

A series of experiment-level analyses and evaluations were conducted to evaluate selectivity and sensitivity and electrochemically monitor the coexisting bioactive molecules on the designed HNC-modified electrode. DPV was performed in the potential ranging from -0.2 V to 0.7 V in 0.1 M PBS (pH 7.0). The DPV results indicate that distinguishable oxidation peak currents were obtained upon simultaneous injections of DA, UA, and AA. The cross-reactivity of individual species was observed by varying its concentration, and the concentration of two other species remains constant. Figure 5c shows that the DA oxidation peak is centered at 0.2 V (vs. Ag/AgCl) and increases linearly upon the addition of DA (1–32 μM) in the presence of AA (0.5 mM) and UA (0.2 mM). The regression equation obtained by plotting the calibration curve of [DA] (μM) versus the peak currents (μA) is given as follows: $I (\mu\text{A cm}^{-2}) = 76.8 [\text{DA}] (\mu\text{M}) + 73.21$; $R^2 = 0.979$; $N = 3$ (Fig. 5d). The detection limit was calculated to be $0.02 \mu\text{M}$ according to $3\sigma/n$, where σ is the slandered error of intercept of the calibration curve, and n is the slope. DA concentrations higher than $32 \mu\text{M}$ show a nonlinear behavior because of DA saturation at active adsorption sites. Similarly, anodic peak current increases linearly at 10–400 and 10–400 μM of AA (Fig. 5a) and UA (Fig. 5e) in the presence of DA (10 μM) and UA (0.2 mM), DA (10 μM) and AA (0.5 mM), respectively. The detection limits of AA and UA on the proposed electrode were determined from the calibration curve of concentrations versus peak currents (Fig. 5b, f). The regression equations are expressed as $I (\mu\text{A cm}^{-2}) = 0.74 [\text{AA}] (\mu\text{M}) + 90.8 \times 10^{-6}$

($R^2 = 0.989$) and $I (\mu\text{A cm}^{-2}) = 1.6 [\text{UA}] (\mu\text{M}) + 85.97$ ($R^2 = 0.957$, $N = 3$) for AA and UA with detection limits of 1.2 and $0.912 \mu\text{M}$, respectively.

For further evidence, DA, AA, and UA were determined simultaneously by DPV in the potential ranging from -0.2 V to 0.6 V in 0.1 M PBS (pH 7.0). Figure 5g shows the DPV anodic peak currents and illustrates the linear behavior with increasing addition of DA, AA, and UA concentrations in the range of 2–60, 10–1000, and 10–800 μM , respectively. As illustrated from Fig. 5h, the detection limits were calculated to be 0.02, 1.127, and $0.978 \mu\text{M}$ for DA, AA, and UA. Evidently, the individual and simultaneous monitoring of these targets were achieved on the HNC-modified electrode with high sensitivity and selectivity. The HNC-modified electrode provides low detection limit and wide linear range for monitoring of AA, DA, and UA as compared to the other modified electrode. Besides that, our modified electrode designed with simple synthesis and without further modification, is presented in Table S1. These results clearly evidenced that the HNC-modified electrode promotes a selective signaling of AA, DA, and UA, where a separate three peaks are obtained, and configuring the electrode selectivity in single and tertiary mixtures as presented in Fig. 5. The HNC possessing intrinsic properties for sensitive and selective monitoring of all targets in one pot may be presented as follows: (i) high catalytic activity resulting from the distinct morphological structure, high surface area, and the atomic arrangement at the surface with direct contact on Ni^{2+} and (ii) fast electron transfer of HNC, and (iii) facile molecular diffusion at the electrode surface. Therefore, the HNC as a modified electrode material may be a promising electrocatalytic material for biosensing applications.

The selectivity of the HNC-modified electrode for monitoring of AA, DA, and UA in the presence of potential interference molecules such as glucose, H_2O_2 , tryptophan, adenine, and guanine that mainly incorporated in the physiological fluid were investigated (Fig. S5). Figure S5a shows the high amperometric response upon addition of 500 μM AA at honest applied potential of 0.01 V in 0.1 M PBS (pH 7). Our finding indicates that there is no any response observed upon the addition of 100 μM DA, 0.1 mM tryptophan, 200 μM UA, 1 mM glucose, 100 μM guanine, and 100 μM adenine molecules to 500 μM AA sensing assays. In addition, the selectivity of DA and UA were performed in the presence of other potentially interfering molecules at honestly applied potential of 0.21 and 0.41 V, respectively, in 0.1 M PBS (pH 7) using the amperometric technique (Fig. S5b, c). The HNC-modified electrode provides a high amperometric response for DA and UA, despite any negligible responses from the other active biomolecules. The findings provide evidence that the HNC-modified electrode exhibits high sensitivity, and selectivity, leading to create a selective signaling of each target of AA, DA, and UA,

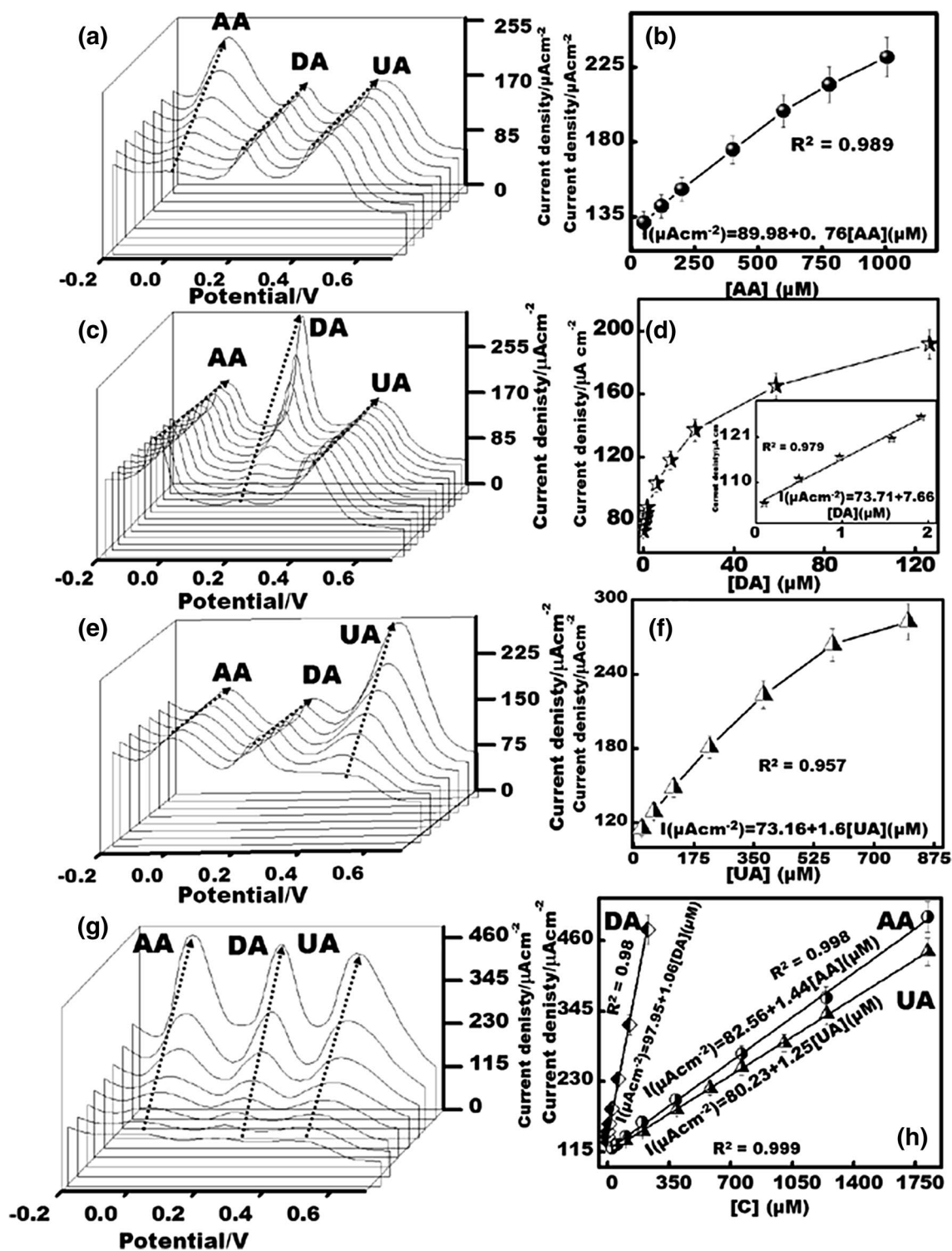


Fig. 5 DPV curves at, **a** increasing concentrations of AA (50–1000 μM) in the presence of 10 μM DA and 0.2 mM UA, **b** the linear plot of concentration of AA (μM) versus current (μA), **c** increasing concentrations of DA (0.1–125 μM) in the presence of 0.5 mM AA and 0.2 mM UA, **d** the linear plot of concentration of DA (μM) versus current (μA), **e** increasing the concentrations of UA (25–800 μM) in the presence of 10 μM DA and 0.5 mM AA, **f** the linear plot of con-

centration of UA (μM) versus current (μA), **g** increasing concentrations of AA (25–1800 μM), DA (2–225 μM), and UA (100–1800 μM), **h** the linear plot of concentration of AA, DA, and UA (μM) versus the current (μA) simultaneously, in N_2 saturated of 0.1 M PBS (pH 7), pulse height 100 mV, pulse width 50 ms, pulse distance 200 ms, and step height 5 mV at HNC-modified electrode

respectively, under one-set screen monitoring in biological fluids.

3.6 One-step signaling of AA, DA, and UA in biological fluids samples at HNC-modified electrode

The uses of the HNC-modified electrode for monitoring of AA, DA, and UA in human biological fluid samples were verified. First, the human urine samples were collected from volunteers and examined using standard addition (age ~ 30 years, the first-morning urination). The urine samples were diluted five times by using PBS (0.1 M, pH 7.0). In brief, 500 μL of the prepared urine sample was added to 9.5 mL of 0.1 M PBS (pH 7). The reliability of the proposed sensor was ascertained by adding certain amounts of AA, DA, and UA to the diluted urine samples and monitored using DPV at room temperature. Investigation of the fresh urine samples indicates the presence of UA (10 μM) and no response for DA and AA at the HNC-modified electrode. The obtained results are presented in Table 1. The recovery of the spiked samples ranged between 97.7 and 105% for AA, DA, and UA. Secondly, the applicability of HNC-modified electrode in the signaling of DA and UA in the human blood serum sample was studied. Known concentrations of AA, DA, and UA were added to the human blood serum solution. The obtained results are presented in Table 2. Investigation of the blood serum samples indicates the presence of UA (2 μM) and no response for DA and AA at the

Table 1 Determination of AA, DA, and UA in human urine samples collected from a volunteer

| Targets | C_A (μM) | C_F (μM) | %R |
|---------|-------------------------|-------------------------|-------|
| AA | 50 | 50 ± 0.03 | 100 |
| | 75 | 76 ± 0.01 | 101 |
| | 100 | 98 ± 0.05 | 98 |
| | 150 | 152 ± 0.05 | 101 |
| DA | 1 | 1.05 ± 0.04 | 105 |
| | 5 | 4.896 ± 0.06 | 97.9 |
| | 10 | 10.128 ± 0.03 | 101.3 |
| | 15 | 14.968 ± 0.091 | 99.7 |
| UA | 25 | 25.124 ± 0.07 | 100.5 |
| | 50 | 50.102 ± 0.093 | 100.2 |
| | 75 | 75.98 ± 0.0572 | 101 |
| | 100 | 105 ± 0.05 | 105 |

The quantitative analyses of targets (AA, DA, and UA) were carried out by spiking all target in one-pot sample with concentration in the range of 1–150 $\mu\text{mol L}^{-1}$. The standardization analyses of targets were determined according to DPV techniques and repeated three times per each sample analysis. Not C_A is concentration of target molecules, C_F is the concentration founded for the molecules, and %R is the percentage of recovery ($\%R = C_F/C_A \times 100$), respectively

Table 2 Determination of AA, DA, and UA in human blood serum samples carried out by spiking all target in the one-pot sample with a concentration in the range of 1–150 $\mu\text{mol L}^{-1}$

| Targets | C_A (μM) | C_F (μM) | %R |
|---------|-------------------------|-------------------------|-------|
| AA | 50 | 49.85 ± 0.003 | 99.7 |
| | 75 | 75.29 ± 0.034 | 100.3 |
| | 100 | 97 ± 0.026 | 97 |
| | 125 | 125.8 ± 0.045 | 100.6 |
| DA | 1 | 1.02 ± 0.003 | 102 |
| | 5 | 4.94 ± 0.004 | 98.9 |
| | 20 | 19.86 ± 0.003 | 99.3 |
| | 50 | 50.19 ± 0.005 | 100.3 |
| UA | 25 | 25.12 ± 0.071 | 100.5 |
| | 50 | 50.3 ± 0.029 | 100.6 |
| | 75 | 74.96 ± 0.072 | 99.9 |
| | 100 | 99.4 ± 0.052 | 99.4 |

The standardization analyses of targets were determined according to DPV techniques and repeated three times per each sample analysis. Not C_A is a concentration of target molecules, C_F is the concentration founded for the molecules, and %R is the percentage of recovery ($\%R = C_F/C_A \times 100$), respectively

HNC-modified electrode. The recovery of the spiked samples ranged from 97 to 100.6, 98.9–102, and 99.4–100.6% for AA, DA, and UA. These results configure that the HNC-modified electrode can be applied for simultaneous detection of AA, DA, and UA in the biological fluid samples.

4 Conclusion

A simple, sensitive, and selective electrochemical biosensor for monitoring of single or multiple bio-components in the biological sample was successfully developed. The HNC-modified electrode provides high electrocatalytic activity as a fact of its morphological construction. The HNC possess a distinct geometry, that is, a rhythmic dual head connected by a stick and the head construction with a thick nanotube. The HNC-modified electrode exhibited remarkable electrocatalytic behavior due to its morphology and massive active site, pore distribution along with dominant {111} plane, dense charge contribution at the surface, and direct catalytic contact with active Ni atom along the top surface. AA, DA, and UA are coexisting molecules in urine and human serum. The HNC-modified electrode exhibited an excellent electrocatalytic oxidation of AA, DA, and UA on one-pot monitoring of single or multiple biomolecules. Simultaneous or individual detection of biomolecules at HNC-modified electrode with high sensitivity up to 0.02, 1.127, and 0.978 μM with a wide linear range of 1–128, 10–000, and 10–800 μM for DA, AA, and UA, respectively, proceeded. The HNC-modified electrode exhibits highly sensitive and selective for one-step

monitoring of AA, DA, and UA in a mixture of different biomolecules. Thus, the HNC-modified electrode can also be employed for real clinical application for detection of multiple biomolecules in a biological fluid sample.

References

- Chen A, Chatterjee S (2013) Nanomaterials based electrochemical sensors for biomedical applications. *Chem Soc Rev* 42(12):5425–5438
- Li B-R, Hsieh Y-J, Chen Y-X, Chung Y-T, Pan C-Y, Chen Y-T (2013) An ultrasensitive nanowire-transistor biosensor for detecting dopamine release from living PC12 cells under hypoxic stimulation. *J Am Chem Soc* 135(43):6034–16037
- Zhang X, Chen X, Kai S, Wang H-Y, Yang J, Wu F-G, Chen Z (2015) Highly sensitive and selective detection of dopamine using one-pot synthesized highly photoluminescent silicon nanoparticles. *Anal Chem* 87(6):3360–3365
- Farjami E, Campos R, Nielsen JS, Gothelf KV, Kjems J, Ferapontova EE (2013) RNA aptamer-based electrochemical biosensor for selective and label-free analysis of dopamine. *Anal Chem* 85:121–128
- Huang J, Liu Y, Hou H, You T (2008) Simultaneous electrochemical determination of dopamine, uric acid and ascorbic acid using palladium nanoparticle-loaded carbon nanofibers modified electrode. *Biosens Bioelectron* 24:632–637
- Jiang J, Du X (2014) Sensitive electrochemical sensors for simultaneous determination of ascorbic acid, dopamine, and uric acid based on Au@Pd-reduced graphene oxide nanocomposites. *Nanoscale* 6:11303–11309
- Wachman ES, Poage RE, Stiles JR, Farkas DL, Meriney SD (2004) Spatial distribution of calcium entry evoked by single action potentials within the presynaptic active zone. *J Neurosci* 24(12):2877–2885
- Cheng F-C, Kuo J-S, Huang H-M, Yang D-Y, Wu T-F, Tsai T-H (2000) Determination of catecholamines in pheochromocytoma cell (PC-12) culture medium by microdialysis–microbore liquid chromatography. *J Chromatogr A* 870:405–441
- Zheng W, Shen B, Zhai W, Gong LR (eds) (2013) *New progress on graphene research*, InTech Publishing Co., Rijeka
- Lapainis T, Scanlan C, Rubakhin SS, Sweedler JV (2007) A multichannel native fluorescence detection system for capillary electrophoretic analysis of neurotransmitters in single neurons. *Anal Bioanal Chem* 387:97–105
- Xu T-Q, Zhang Q-L, Zheng J-N, Lv Z-Y, Wei J, Wang A-J, Feng J-J (2014) Simultaneous determination of dopamine and uric acid in the presence of ascorbic acid using Pt nanoparticles supported on reduced graphene oxide. *Electrochim Acta* 115:109–115
- Sun JY, Gan T, Deng YP, Shi ZX, Lv Z (2015) Pt nanoparticles-functionalized hierarchically porous γ -Al₂O₃ hollow spheres based electrochemical sensor for ultrasensitive guaiacol detection. *Sens Actuators B* 211:339–345
- Zhang YY, Gan T, Wan CD, Wu KB (2013) Morphology-controlled electrochemical sensing amaranth at nanomolar levels using alumina. *Anal Chim Acta* 764:53–58
- Wu C, Tang Y, Wan CD, Liu HY, Wu KB (2015) Enhanced-oxidation and highly-sensitive detection of acetaminophen, guanine, and adenine using NMP-exfoliated graphene nanosheets-modified electrode. *Electrochim Acta* 166:285–292
- Qu Y, Ma M, Wang Z, Zhan G, Li B, Wang X, Fang H, Zhang H, Li C (2013) Sensitive amperometric biosensor for phenolic compounds based on graphene–silk peptide/tyrosinase composite nanointerface. *Biosens Bioelectron* 44:85–88
- Yang YJ, Li W (2014) CTAB functionalized graphene oxide/multiwalled carbon nanotube composite modified electrode for the simultaneous determination of ascorbic acid, dopamine, uric acid and nitrite. *Biosens Bioelectron* 56:300–306
- Fernandes DM, Costa M, Pereira C, Bachiller-Baeza B, Rodríguez-Ramos I, Guerrero-Ruiz A, Freire C (2014) Novel electrochemical sensor based on N-doped carbon nanotubes and Fe₃O₄ nanoparticles: Simultaneous voltammetric determination of ascorbic acid, dopamine and uric acid. *J Colloidal Interfaces Sci* 432:207–213
- Abdelwahab AA, Shim Y-B (2015) Simultaneous determination of ascorbic acid, dopamine, uric acid and folic acid based on activated graphene/MWCNT nanocomposite loaded Au nanoclusters. *Sens Actuators B* 221:659–665
- Cai W, Lai J, Lai T, Xie H, Ye J (2016) Controlled functionalization of flexible graphene fibers for the simultaneous determination of ascorbic acid, dopamine and uric acid. *Sens Actuators B* 224:225–232
- Zhang X, Zhang Y-C, Ma L-X (2016) One-pot facile fabrication of graphene-zinc oxide composite and its enhanced sensitivity for simultaneous electrochemical detection of ascorbic acid, dopamine and uric acid. *Sens Actuators B* 227:488–496
- Palanisamy S, Thirumalraj B, Chen S-M, Ali MA, Al-Hemaid FMA (2015) Palladium nanoparticles decorated on activated fullerene modified screen printed carbon electrode for enhanced electrochemical sensing of dopamine. *J Colloidal Interfaces Sci* 448:251–256
- Wang Y, Huang Y, Wang B, Fang T, Chen J, Liang C (2016) Three-dimensional porous graphene for simultaneous detection of dopamine and uric acid in the presence of ascorbic acid. *J Electroanal Chem* 782:76–83
- Wang C, Li J, Shi K, Wang Q, Zhao X, Xiong Z, Zou X, Wang Y (2016) Graphene coated by polydopamine/multi-walled carbon nanotubes modified electrode for highly selective detection of dopamine and uric acid in the presence of ascorbic acid. *J Electroanal Chem* 770:56–61
- Ojani R, Raoof JB, Maleki AA, Safshekan S (2014) Simultaneous and sensitive detection of dopamine and uric acid using a poly(L-methionine)/gold nanoparticle-modified glassy carbon electrode. *Chin J Catal* 35:423–442
- Hu H, Song Y, Feng M, Zhan (2016) Carbon nanomaterials for simultaneous determination of dopamine and uric acid in the presence of ascorbic acid: from one-dimensional to the quasi one-dimensional. *Electrochim Acta* 190:40–48
- Ghanbari Kh, Moludi M (2016) Flower-like ZnO decorated polyaniline/reduced graphene oxide nanocomposites for simultaneous determination of dopamine and uric acid. *Anal Biochem* 512:91–102
- Sun CL, Lee HH, Yang JM, Wu CC (2011) The simultaneous electrochemical detection of ascorbic acid, dopamine, and uric acid using graphene/size-selected Pt nanocomposites. *Biosens Bioelectron* 26(8):3450–3455
- Zhang X, Yan W, Zhang J, Li Y, Tang W, Xu Q (2015) NiCo-embedded in hierarchically structured N-doped carbon nanoplates for the efficient electrochemical determination of ascorbic acid, dopamine, and uric acid. *RSC Adv* 5:65532–65539
- El-Safty SA, Kiyozumi Y, Hanaoka T, Mizukami F (2008) Nanosized NiO particles wrapped into uniformly mesocaged silica frameworks as effective catalysts of organic amines. *Appl Catal A* 337(2):121–129
- Shenashen MA, Hassen D, El-Safty SA, Isago H, Elmarakbi A, Yamaguchi H (2017) Axially oriented tubercle vein and X-crossed sheet of N-Co₃O₄@C hierarchical mesoarchitectures as potential heterogeneous catalysts for methanol oxidation reaction. *Chem Eng J* 313:83–98

31. Shenashen MA, Hassen D, El-Safty SA, Selim MM, Akhtar N, Chatterjee A, Elmarakbi A (2016) Mesoscopic fabric sheet racks and blocks as catalysts with efficiently exposed surfaces for methanol and ethanol electrooxidation. *Adv Mater Interfaces* 3(24):1600743
32. Gomaa H, Khalifa H, Selim MM, Shenashen MA, Kawada S, Alamoudi AS, Azzam AM, Alhamid AA, El-Safty SA (2017) Selective, photo-enhanced trapping/detrapping of arsenate anions using mesoporous blobfish head TiO₂ monoliths. *ACS Sustain Chem Eng* 5(11):10826–10839
33. Azzam AM, Shenashen MA, Selim MM, Yamaguchi H, El-Sewify IM, Kawada S, Alhamid AA, El-Safty SA (2017) Nanospherical inorganic α -Fe core-organic shell necklaces for the removal of arsenic (V) and chromium (VI) from aqueous solution. *J Phys Chem Solids* 109:78–88
34. Selim MS, Elmarakbi A, Azzam AM, Shenashen MA, EL-Saeed AM, El-Safty SA (2018) Eco-friendly design of superhydrophobic nano-magnetite/silicone composites for marine foul-release paints. *Prog Org Coat* 116:21–34
35. Selim MS, Shenashen MA, Elmarakbi A, El-Saeed AM, Selim MM, El-Safty SA (2017) Sunflower oil-based hyperbranched alkyd/spherical ZnO nanocomposite modeling for mechanical and anticorrosive applications. *RSC Adv* 7:21796–21808
36. Selim MS, Shenashen MA, Elmarakbi A, Fathallah NA, Hasegawa S-i, El-Safty SA (2017) Synthesis of ultrahydrophobic and thermally stable inorganic–organic nanocomposites for self-cleaning foul release coatings. *Chem Eng J* 320:653–666
37. El-Safty SA, Sakai M, Selim MM, Hendi AA (2015) Mesosponge optical sinks for multifunctional mercury ion assessment and recovery from water sources. *ACS Appl Mater Interfaces* 7(24):13217–13231
38. Khairy M, El-Safty SA (2013) Mesoporous NiO nanoarchitectures for electrochemical energy storage: influence of size, porosity, and morphology. *RSC Adv* 3(45):23801–23809
39. Khairy M, El-Safty SA, Ismael M, Kawarada H (2012) Mesoporous NiO nanomagnets as catalysts and separators of chemical agents. *Appl Catal B* 127:1–10
40. Akhtar N, El-Safty SA, Abdelsalam ME, Kawarada H (2015) One-pot fabrication of dendritic NiO@carbon–nitrogen dot electrodes for screening blood glucose level in diabetes. *Adv Healthc Mater* 4(14):2110–2119
41. Akhtar N, El-Safty SA, Abdelsalam ME, Shenashen MA, Kawarada H (2016) Radially oriented nanostrand electrodes to boost glucose sensing in mammalian blood. *Biosens Bioelectron* 77:656–665
42. Akhtar N, Emran MY, Shenashen MA, Khalifa H, Osaka T, Faheem A, Homma T, Kawarada H, El-Safty SA (2017) Fabrication of Photo-electrochemical biosensor for ultrasensitive screening of mono-bioactive molecules: effect of geometrical structures and crystal surfaces. *J Mater Chem B* 5:7985–7996
43. Zhang X, Shi W, Zhu J, Zhao W, Ma J, Mhaisalkar S, Maria T, Yang Y, Zhang H, Hng H, Yan Q (2010) Synthesis of porous NiO nanocrystals with controllable surface area and their application as supercapacitor electrodes. *Nano Res* 3:643–652
44. Hassan D, El-Safty SA, Khalil KA, Dewidar M, Abu El-Maged G (2016) Mesoporous carbon/Co₃O₄ hybrid as efficient electrode for methanol electrooxidation in alkaline conditions. *Int J Electrochem Sci* 11:8374–8390
45. Khairy M, El-Safty SA (2014) Nanosized rambutan-like nickel oxides as electrochemical sensor and pseudocapacitor. *Sens Actuators B* 193:644–652
46. El-Sewify IM, Shenashen MA, Shahat A, Yamaguchi H, Selim MM, Khalil MM, El-Safty SA (2017) Ratiometric fluorescent chemosensor for Zn²⁺ ions in environmental samples using supermicroporous organic–inorganic structures as potential platforms. *ChemistrySelect* 2:11083–11090
47. Shenashen MA, El-Safty SA, Khairy M (2013) Trapping of biological macromolecules in the three-dimensional mesocage pore cavities of monolith adsorbents. *J Porous Mater* 20:679–692
48. Shenashen MA, Elshehy EA, El-Safty SA, Khairy M (2013) Visual monitoring and removal of divalent copper, cadmium, and mercury ions from water by using mesoporous cubic Ia3d aluminosilica sensors. *Sep Pur Techn* 116:73–86
49. Shenashen MA, El-Safty SA, Elshehy EA (2014) Monolithic scaffolds for highly selective ion sensing/removal of Co(II), Cu(II), and Cd(II) ions in water. *Analyst* 139:6393–6405
50. Shenashen MA, El-Safty SA, Elshehy EA (2014) Synthesis, morphological control, and properties of silver nanoparticles in potential applications. *Part Part Syst Charact* 31:293–316
51. Zhuo K, Jeong M-G, Chung C-H (2013) dendritic nanoporous nickel oxides for a supercapacitor prepared by a galvanic displacement reaction with chlorine ions as an accelerator. *RSC Adv* 3:12611–12615
52. Hassen D, El-Safty SA, Tsuchiya K, Chatterjee A, Elmarakbi A, Shenashen MA, Sakai M (2016) Longitudinal hierarchy Co₃O₄ mesocrystals with high-dense exposure facets and anisotropic interfaces for direct-ethanol fuel cells. *Sci Rep* 6:24330
53. El-Safty SA, Kiyozumi Y, Hanaoka T, Muzukami F (2014) Heterogeneous catalytic activity of NiO-silica composites designed with cubic *Pm3n* cage nanostructures. *Appl Catal B* 82:169–179
54. Shenashen MA, Akhtar N, Selim MM, Morsy WM, Yamaguchi H, Kawada S, Alhamid AA, Ohashi N, Ichinose I, Alamoudi AS, El-Safty SA (2017) Effective, low-cost recovery of toxic arsenate anions from water by using hollow-sphere geode traps. *Chem Asian J* 12(15):1952–1964
55. Shenashen MA, Kawada S, Selim MM, Morsy WM, Yamaguchi H, Alhamid AA, Ohashi N, Ichinose I, El-Safty SA (2017) Bushy sphere dendrites with husk-shaped branches axially spreading out from the core for photo-catalytic oxidation/remediation of toxins. *Nanoscale* 9:7947–7959
56. Emran MY, Shenashen MA, Mekawy M, Azzam AM, Akhtar N, Gomaa H, Selim MM, Faheem A, El-Safty SA (2018) Ultrasensitive in-vitro monitoring of monoamine neurotransmitters from dopaminergic cells. *Sens Actuators B* 259:114–124
57. Emran MY, Mekawy M, Akhtar N, Shenashen MA, EL-Sewify IM, Faheem A, El-Safty SA (2018) Broccoli-shaped biosensor hierarchy for electrochemical screening of noradrenaline in living cells. *Biosens Bioelectron* 100:122–131
58. Emran MY, Khalifa H, Gomaa H, Shenashen MA, Akhtar N, Mekawy M, Faheem A, El-Safty SA (2017) Hierarchical CN doped NiO with dual-head echinop flowers for ultrasensitive monitoring of epinephrine in human blood serum. *Microchim Acta* 184(11):4553–4562
59. Laviron E (1979) General expression of the linear potential sweep voltammogram in the case of diffusionless electrochemical systems. *J Electroanal Chem Interfacial Electrochem* 101:19–28
60. Chen L, Feng M, Zhan H (2014) Fundamental electrochemistry of three-dimensional graphene aerogels. *RSC Adv* 4:30689–30696
61. Kim SJ, Kim YL, Yu A, Lee J, Lee SC, Lee C, Kim MH, Lee Y (2014) Electrospun iridium oxide nanofibers for direct selective electrochemical detection of ascorbic acid. *Sens Actuators B* 196:480–488
62. Pisoschi AM, Pop A, Serban AI, Fafaneata C (2014) Electrochemical methods for ascorbic acid determination. *ElectrochimActa* 121:443–460
63. Zhao DY, Fan DW, Wang JP, Xu CX (2015) Hierarchical nanoporous platinum-copper alloy for simultaneous electrochemical determination of ascorbic acid, dopamine, and uric acid. *MicrochimActa* 182:1345–1352

64. Granero AM, Pierini GD, Robledo SN, Di Nezio MSD, Fernández H, Zon MA (2016) Simultaneous determination of ascorbic and uric acids and dopamine in human serum samples using three-way calibration with data from square wave voltammetry. *Microchem J* 129:205–212
65. Wang W, Xu G, Cui XT, Sheng G, Luo X (2014) Enhanced catalytic and dopamine sensing properties of electrochemically reduced conducting polymer nanocomposite doped with pure graphene oxide. *Biosens Bioelectron* 58:153–156

Affiliations

Mohammed Y. Emran^{1,2} · Mohamed A. Shenashen¹ · Adel A. Abdelwahab² · Hesham Khalifa¹ · Moataz Mekawy¹ · Naeem Akhtar¹ · Mohamed Abdelmottaleb² · Sherif A. El-Safty^{1,3}

✉ Sherif A. El-Safty
sherif.elsafty@nims.go.jp; sherif.el-safty@sunderland.ac.uk

¹ Research Centre for Functional Materials, National Institute for Materials Science (NIMS), 1-2-1 Sengen, Tsukuba-shi, Ibaraki-ken 305-0047, Japan

² Department of Chemistry, Faculty of Science, Al-Azhar University, Assiut 71524, Egypt

³ Faculty of Engineering and Advanced Manufacturing, University of Sunderland, St Peter's Campus, Sunderland SR6 0DD, UK